2023 IEEE International Conference on Robotics and Automation (ICRA 2023)
May 29 - June 2, 2023. London, UK

Hummingbird-bat hybrid wing by 3-D printing*

Tomoya Fujii, Jinqiang Dang, and Hiroto Tanaka

Abstract— **Hovering hummingbirds have inspired small flapping-wing aerial robots. Natural flyers, including hummingbirds and bats, undergo torsional wing deformation during flapping flight owing to complex wing structure, while previous artificial wings were relatively simple and difficult to design the torsional flexibility. In this paper, we proposed a hummingbird-bat hybrid (HBH) wing in which torsional flexibility was implemented by an available fabrication technology. The HBH wing had a torsional arm at the leading edge inspired by a torsional wrist of a hummingbird. A bat-like stretchable wing membrane was also employed not to constrain the wing torsion. The membrane was supported by wing shafts of which bending stiffness was designed based on that of the feather shaft of a hummingbird. The three-dimensional (3-D) shape of the torsional arm and wing shafts was created by 3-D printing. The effect of the torsional arm and stretchable membrane on lift generation and deformation was evaluated using an electric flapping mechanism. It was confirmed that the torsional arm actually enhanced the passive wing torsion. The stretchable wing membrane further promoted the torsion effect of the torsional arm. Consequently, the HBH wing did not increase lift, but efficacy, defined as lift per input power, was greatly improved by 14% at most compared with the wing without a torsional arm.**

I. Introduction

Hummingbirds are the only bird species that can hover continuously and have excellent flight capabilities, including rapid acceleration and sharp turns. Therefore, small flapping flight robots based on hummingbirds have been studied [1−11]. Wings of bats, insects, and flying birds including hummingbirds are flexible and are deformed by aerodynamic and inertial forces. Torsional and camber deformation of wings during flapping flight contributes to lift efficacy and robustness to changing wind conditions [12−15]. The wing structure that achieves proper deformation varies among organisms. In hummingbird wings, torsion of the wing surface is realized by passive bending and sliding of the separate wind fin feathers that make up the wing surface [15]. Rotation around the anterior edge of the wrist joint on the root side of the anterior margin of the wing also contributes to torsional deformation [16]. In bats, the wing surface consists of an elastic wing membrane stretched between the phalanges, which can actively change the camber [17].

*Research supported by JSPS KAKENHI Grant-in-Aid for Scientific Research on Innovative Areas "Science of Soft Robots" project under Grant Number JP18H05468.

The authors are with Tokyo Institute of Technology, Tokyo, Japan.
Hiroto Tanaka is a corresponding author to provide e-mail: tanaka.h.cb@m.titech.ac.jp.

On the other hand, the wings of conventional hummingbird-norm flapping robots are simpler than biological wings [1−4]. Most artificial wings consist of a polymer film supported by a relatively stiff frame, consisting of materials such as carbon fiber-reinforced plastic (CFRP). The wing deformation during flapping has also not been studied in detail. Our research group has developed artificial wing shafts that mimicked the static bending stiffness of the wing shafts of a hummingbird specimen's wind fin feathers [18, 19]. However, the non-stretchy wing membrane could not achieve as much twist as a hummingbird.

In this study, we propose a hummingbird-bat hybrid wing that incorporates a hummingbird's rotating wrist joint and a bat's elastic wing membrane, in addition to hummingbird-mimetic wing shafts, to achieve the twisting deformation shown by actual hummingbird wings. This wing is designed for hummingbird-like flapping flight and has a twistable structural mechanism on the leading edge corresponding to a wrist joint. The wing membrane is made of a thin elastomeric film that is stretchable like a bat's. The single-wing membrane is easy to fabricate, and its stretchability allows a more significant wing surface torsion. Camber formation, as seen in bat wings, is also expected.

3-D printing was employed to fabricate the torsion structure of the leading edge and the hummingbird-like wing shafts as a single unit. Using a printer capable of simultaneously printing multiple materials with vastly different physical properties, the low-rigidity and high-rigidity parts of the wing shafts and the torsional arm which were designed three-dimensionally were integrated. The one-piece formation eliminated the need for manual assembly using adhesives, resulting in higher precision and weight reduction. Furthermore, the design, prototyping, testing, and evaluation cycles were shortened.

The following sections describe the structure of the hummingbird-bat hybrid wing, its fabrication method, and measurements of wing deformation, lift, and efficacy through flapping experiments.

II. Artificial Wing Design and Fabrication Method

A. Wing membrane and wing frame

The hummingbird-bat hybrid (HBH) wing in this study consists of a stretchable wing membrane and a 3-D printed wing frame composed of four wing shafts, a wing base, and a torsional arm (Fig. 1). The stretchable membrane was inspired

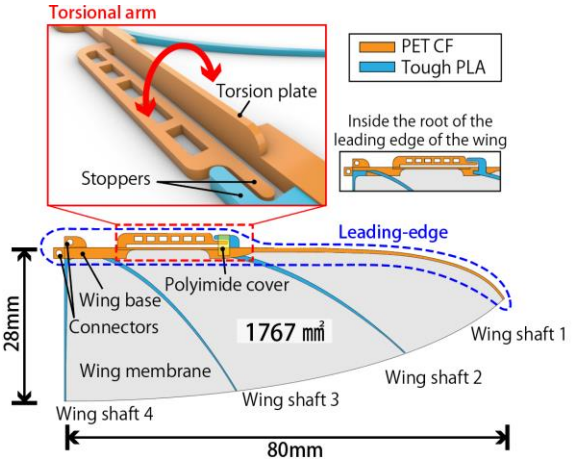

Figure 1 Design and structure of hummingbird-bat hybrid (HBH) wing.

by the bat wing, and the torsional arm and wing shafts were inspired by the wrist joint and feather shafts of the hummingbird wing, respectively. The wing outline shape was the same as a real Amazilia hummingbird (*Amazilia amazilia*) [15].

8-µm-thick polyurethane elastomer film (Silklon NES85, Okura Industrial Co., Ltd., Japan) was used for the stretchable membrane The 3-D printed wing frame was manually glued to the membrane with elastic adhesive (Super X Hyper Wide, Cemedine Co., Ltd., Japan).

Ultimaker S5 (Ultimaker B.V., The Netherlands) and two types of material were used to fabricate the wing frame. PLA (polylactide) (Black Tough PLA, Ultimaker B.V., The Netherlands) was used for the wing shaft 2 to 4, and PET CF (carbon fiber reinforced polyethylene terephthalate) (3F PET CF 9780 BK, Lehmann & Voss & Co. KG., Germany) was used for the other parts. Young's modulus, E, and print settings are shown in Table 1. Each E was taken from the product data sheet. E for PET CF was 2.86 times greater than that of PLA (Table 1).

The bending stiffness of the wing shafts was designed based on the results of static bending tests of real feather shafts of a museum specimen of Amazilia hummingbird [19]. The bending stiffness, EI, was expressed as a function of the distance from the shaft tip, x [mm], as

$$EI = k \times 10^{-9} x^{a} \quad (1) \ ,$$

where k and a were determined for each wing shaft as shown in Table 2 through trial flapping experiments to achieve high lift. The cross-section of the wing shaft was designed to be square, and width h was tapered from the base to tip to follow the above bending stiffness function. To secure practical strength, the minimum width and thickness at the shaft tip were decided as shown in Table 2. The cross-section of the wing base was rectangular of which width and thickness were 2 mm and 0.9 mm, respectively.

Despite the above fine detail of the wing frame, the printing time was only 1 hour with a high precision printing setting shown in Table 1.

Table 1 Young's modulus and 3-D printing setting of each material

Material	Tough PLA	PET CF
Young's modulus, E [GPa]	2.8	8
Shear modulus, G [GPa]	-	1
Print core type	AA0.25	CC0.4
Layer height [mm]	0.05	0.05
Line width [mm]	0.2	0.34
Printing temperature [°C]	205	275
Print speed [mm/sec]	40	30

Table 2 Design parameters of wing shafts

	Wing shaft 1	**Wing shaft 2**	**Wing shaft 3**	**Wing shaft 4**
k	9	10	5.2	4.6
a	2.7	2.5	2.5	2.5
Minimum width [µm]	450	250	250	250
Minimum thickness [µm]	250	150	150	150

B. Torsional arm

The torsional arm realizes torsion along with the wing axis with a torsional rectangular plate (Fig. 1). Chordwise bending was limited by the contact of the stoppers. To secure the contact, the stoppers were covered with 12.5-µm-thick polyimide film (Kapton 50H, DU PONT-TORAY CO., LTD., Japan).

The torsional stiffness of the torsion plate can be calculated as follows. The torsional stiffness k_R of a rectangular plate of a [m] width and b [m] thickness where $a < b$ can be expressed as

$$k_R = GJ \quad (2) \ ,$$

where G [Pa] is a shear modulus of elasticity and J [m^4] is a shape factor of the cross section. The J can be expressed as

$$J = \frac{a^3 b}{3}\left[1 - \frac{192}{\pi^5}\left(\frac{a}{b}\right)\sum_{n=1,3,5,\cdots}^{\infty}\frac{1}{n^5}\tanh\frac{n\pi b}{2a}\right] \quad (3) \ ,$$

for rectangular cross section [20,21].

The cross-section of the torsion plate was 0.4 mm in width and 2 mm in thickness. The G of PET CF was calculated from static torsion measurement of a test plate (length: 18.4 mm; width 14.7 mm; thickness: 1.7 mm) with a torque gauge, resulting in 1 [GPa]. Thus, the torsional stiffness of the torsion plate was calculated to be 4.27×10^{-5} [Nm^2] from Equations (2) and (3).

C. Wing asymmetry

The wing frame (the rib and the wing shafts) was glued only on the back side of the wing membrane, while the front side of the membrane is clean. Hence, the wing is asymmetrical in the front-back direction. The wing frame is also asymmetrical because it was flat on the membrane side and printed towards the other side. A downstroke was defined as a stroke from the front side (membrane side) to the back side (wing frame side), and an upstroke was defined as the counterstroke.

D. Artificial wings for comparison

To compare the effect of the torsional arm and the effect of the stretchy wing membrane, three types of wings were fabricated including the hummingbird-bat hybrid wing (HBH wing), the Non-torsion wing that has a stretchy wing

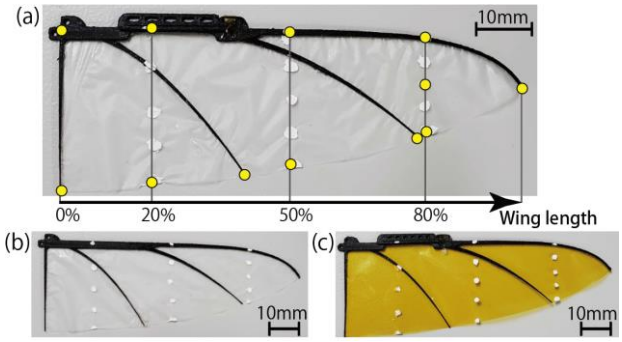

Figure 2 Fabricated wings viewed from the back side. (a) HBH wing (b) Non-torsion wing (c) Non-stretch wing. Yellow dots indicate the positions measured in the motion analysis.

Table 3 Mass of the wings.

Wing	HBH wing	Non-torsion wing	Non-stretch wing
Original wing	186 [mg]	181 [mg]	204 [mg]
Marked wing	194 [mg]	189 [mg]	215 [mg]

membrane but no torsional arm, and the Non-stretch wing that has a non-stretchy wing membrane and a torsional arm (Fig. 2). The Non-torsion wing has a rectangular body with an extended wing base in place of a torsional arm, eliminating stoppers. The torsional stiffness of the extended part is 11.4 times that of the torsional arm. For the Non-stretch wing, a 12.5 μm thick polyimide film was used instead of the 8 mm thick urethane elastomer film used in the HBH wing. The weight of the wing was increased after adding markers for motion analysis. Table 3 shows the weights of each wing before and after adding markers.

III. Flapping Experiment

A. Experimental method

Only a left wing which has the wing root on the right side when the wing membrane side is up was attached to the flapping mechanism to measure lift and wing deformation during flapping (Fig. 3). The mechanism was driven by a DC motor with a constant voltage supplied by a DC power supply. The rotation of the motor was firstly reduced by a two-stage planetary gear reducer with a reduction ratio of 16 and then converted to the reciprocating motion of a slider via a pin-slot mechanism. The slider has a rack gear on each side, rotating a pinion gear to which a spanwise shaft was fixed. The flapping amplitude was designed to be 158°. The feathering rotation around the spanwise shaft was limited to ±20° by a stopper as shown in Fig. 3. The feathering limitation (20°) is similar to the maximum feathering during upstroke of our model hummingbird (18°), while the flapping amplitude is larger than that of the model hummingbird (108°). *Re* (Reynolds number) at the mid stroke with 17.5-Hz flapping ($Re \approx 1.8 \times 10^4$) is similar to that of the model hummingbird ($Re \approx 1.8 \times 10^4$ at 28.8 Hz), where the representative length is the wing length and the representative speed is the moving speed at wingtip at the mid stroke.

The flapping mechanism was tethered on an electronic balance (UW1020H, Shimadzu Corporation, Japan) via vertical support to measure the time average lift during flapping (Fig. 4). The support height was set to be more than

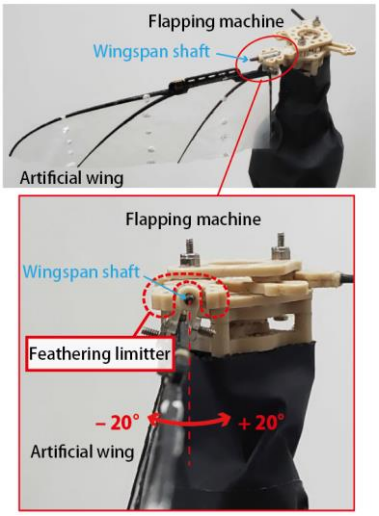

Figure 3 Flapping machine and feathering limiter.

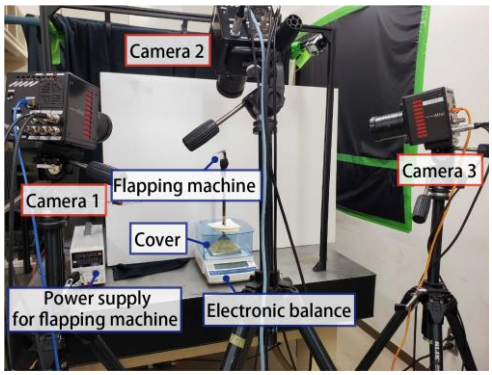

Figure 4 Experimental setup.

2.5 times the flapping radius to avoid ground effects. The balance was covered to avoid the influence of the downward flow on the sensing of the balance. The flapping frequency was manually adjusted to be 15, 17.5, 20, 22.5, and 25 Hz with the input voltage value. Consequently, *Re* ranged from 1.5×10^4 to 2.5×10^4. Input power was calculated from the voltage and current displayed on the power supply (PA18-2B, TEXIO TECHNOLOGY CORPORATION, Japan).

The efficacy of lift generation, η, was defined as

$$\eta = \frac{F}{P} \quad (4) \ ,$$

where, F [N] is the time average lift, and P [W] is the input power [22]. Thus, η has a unit of N/W.

Wing deformation was measured by motion analysis of the markers on the wing. The wing was flapped at 25 Hz and captured with three synchronized high-speed video cameras (Fastcam-MiniAX100, PHOTRON LIMITED, Japan) with 50 mm lenses. The frame rate, exposure time, and resolution were 2000 frames/s, 1/10000 s, and 1024 pixels × 1024 pixels, respectively. The flapping frequency is 25 Hz, so there are 80 frames per stroke, but only even-numbered frames were used in this study. The markers and features of the wing used for motion analysis were the ends of the wing chords at 0%, 20%, 50%, and 80% of the wing length, the distal tips of the wing shafts, and the center point of the wing chord at 80% of the

wing length (Fig. 2 (a)). 3-D positions of the above markers and feature points were calculated with commercial motion analysis software using DLT (direct linear translation) method (DIPP-MotionV, DITECT Co., Ltd., Japan).

Three discrete wingbeats were selected from a single sequence of continuous wingbeats for the motion analysis. Mid-downstroke period and mid-upstroke period were defined as the periods from $t = 0.15\ T$ to $0.35\ T$ and from $t = 0.65\ T$ to $0.85\ T$), respectively, where T is the duration of the single wingbeat (0.04 s). The timing of $t = 0$ was defined as the timing when the slider starts to move from the end position of the travel distance. In the following analysis, each time-series kinematics data was ensemble-averaged using the data from three wingbeats.

The wing deformation was investigated on the wing coordinate fixed to the wing base. In this coordinate system, the *Y*-axis is defined as the axis connecting the leading edge points at the 20% and 50% positions of the wing length, and the *Z*-axis is the axis onto which the vertical downward vector is projected on the plane perpendicular to the *Y*-axis (hereafter called as wing section plane), and the *X*-axis is the direction of the cross product of the *Y* and *Z*-axes (Fig. 5 (a)). To evaluate the rotation of each chord around the *Y*-axis, each trailing edge point was projected onto the plane perpendicular to the *Y*-axis (Fig. 5 (a)). The wing chord center point at 80% of the wing length was projected in the same way.

The feathering angle, wing velocity vector, angle of attack, angle of twist, and camber ratio were obtained from the positional data on the wing coordinate system. The feathering angle is the angle of the wing chord to the vertical direction, the wing velocity vector is the vector of the velocity at the leading edge point of each wing chord, the angle of attack is the angle of the wing chord to the velocity vector, the angle of twist is the difference between the feathering angles of each wing chord, and the camber ratio is defined as the ratio of the distance between the wing chord center point and the wing chord, which is defined as camber, divided by the wing chord length (Fig. 5 (b)). The positive directions of the feathering angle and the angle of attack are counterclockwise and clockwise when looking from the wingtip side to the wing root side, respectively. The camber is positive when the wing expands in the opposite direction of wing movement.

In order to evaluate the twist of the wing frame eliminating the effects of bulging of the wing membrane, virtual trailing-edge markers were generated by taking the intersection of the wing plane and the line connecting the tips of the wing shafts (Fig. 5 (a)). The virtual trailing-edge points were used for the calculation of the feathering angle and the angle of twist in the following analysis.

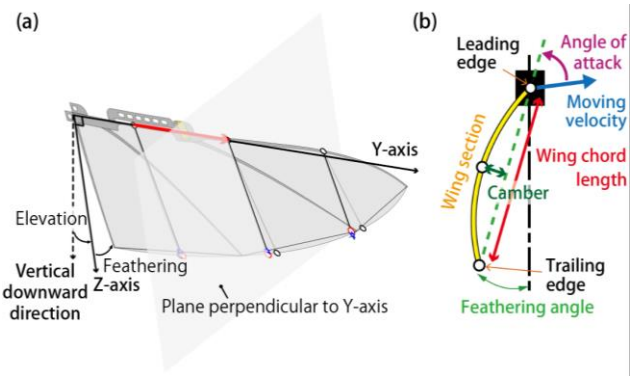

Figure 5 (a) Wing coordinate system, wing section plane, and trailing edge points for motion analysis (black circle: original trailing edge point, red circle: projected trailing edge point, blue star: virtual trailing edge point). (b) Measured parameters on the wing section plane.

B. Average lift and efficacy results

Fig. 6 shows the measured time-average lift and efficacy. The efficacy of the HBH wing was more than 14% higher than that of the Non-torsion wing and more than 8% higher than that of the Non-stretch wing at all frequencies studied. On the contrary, the lift of the HBH wing at flapping frequencies of 20 Hz or more was smaller than the other wings by 7% at most.

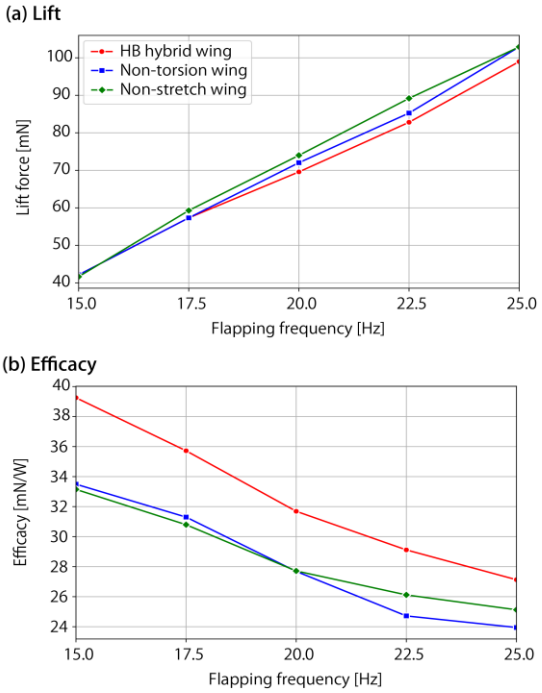

Figure 6 Time-average lift (a) and efficacy (b).

Table 4 Comparison with a hummingbird wing and other hummingbird-sized wings

	Wing length [mm]	Wing area [mm^2]	Lift [mN]	Flapping frequency [Hz]	Flapping amplitude [degree]	Lift per wing area [N/m^2]
HBH wing	80	1767	42.1 / 99.0	15 / 25	158	23.8 / 56.0
ASL robot [1]	90	1750	85.8	25	180	49
Nano-hummingbird [2]	68	1768	87.5	27.5	180	49.5
Maryland hummingbird [3]	140	9232	308.3	20	120	33.4
KUBeetle S [5]	100	2064	77.4	18	190	37.5
Hummingbird [15, 23]	70	1406	27.4	28.8	110	19.5

The comparison of the HBH wing with a real hummingbird and other hummingbird-sized hovering robots is summarized in Table 4. The HBH wing at 25 Hz frequency achieved the highest lift per wing area among them.

C. *Effect of the torsional arm and the stretchy membrane*

The ensemble-averaged feathering angles at 25-Hz flapping are shown in Fig. 7. The average standard deviations of the feathering angles were about 6.0, 4.1, 2.8, and 3.2 for 80%, 50%, 20%, and 0% wing length positions, respectively. For all the wings, the distal chord tended to feather more than the proximal chord during each stroke, indicating a wing twist in the direction of wing length.

The effect of the torsional arm on the wing twist was revealed by comparing the HBH with the Non-torsion wings. The average angle of twist from 20% to 80% positions of the wing length across the torsional arm of the Non-torsion wing was 35% smaller in the mid-downstroke period and 44% smaller in the mid-upstroke period than that of the HBH wing (Table 5). On the other hand, the twist angle from 0% to 20% of the wing length was almost the same. The presence or absence of the torsional arm has little effect on the position without the torsional arm. Thus, the torsional arm promoted the twist of the wing tip. Note that mid-upstroke period caused more twist despite the symmetric flapping motion (Table 5). This might be due to the asymmetry of the wing structure explained in subsection II C.

The effect of the stretchable wing membrane on the wing twist was clarified by comparing the HBH wing with the Non-stretch wing. The average angle of twist from 20% to 80% of wing length for the Non-stretch wing was 18% smaller in the mid-downstroke period and 32% smaller in the mid-upstroke period than that of the HBH wing (Table 5). That is, the stretchable membrane was needed to maximize the effect of the torsional arm. On the contrary, the angle of twist from 0% to 20% of wing length for the Non-stretch wing was 30% larger in the mid-downstroke period and 37% larger in the mid-upstroke period than that of the HBH wing (Table 5). It might be because the high tension by the torsion of the non-stretch membrane at this 20% to 80% area pulled the wing shaft 3 inward so that the twist was allowed.

The stretchable wing membrane also enhanced the camber. Time-average camber ratio of the two wings with the stretchable membrane (HBH and Non-torsion) was larger than that of the Non-stretch wing (Table 6). Note that the camber ratios of all wings were positive and were larger than that of a real hummingbird [15]. The large camber may contribute to stall delay on the artificial wing, which has a larger angle of attack than the actual hummingbird (Table 7), but it may also result in slightly higher drag.

D. *Relationship between wing deformation and lift efficacy*

The HBH wing underwent the largest twist and achieved the highest efficacy in lift generation in the present study, which agrees with the previous study reporting that the larger the torsion leads to the higher the efficacy [12]. The largest twist of the HBH wing resulted in the smallest angle of attack at the distal region (80% wing length position) as shown in Table 7. In general, an excess angle of attack leads to a large drag. Thus, the highest efficacy of the HBH wing can be attributed to the reduction of the excess angle of attack. Note that the difference in the angle of attack at 80% wing length position between HBH and Non-stretch wings was small for mid-downstroke period (Table 7). This is assumed to be due to a small difference in the twist angle for the mid-downstroke

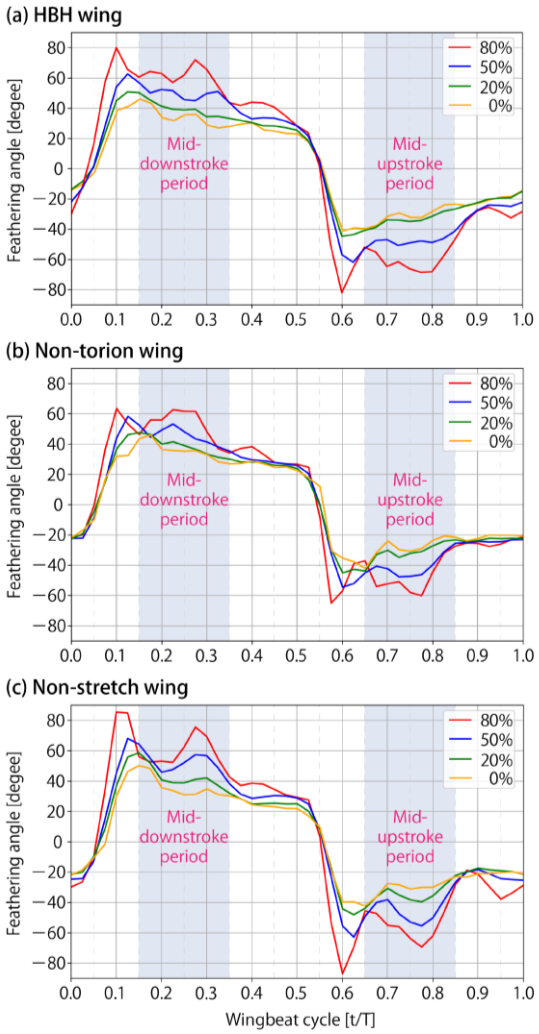

Figure 7 Time variation of feathering angles at 0%, 20%, 50%, and 80% wing length positions. Flapping frequency was 25 Hz.

Table 5 Average angle of twist for proximal (0% to 20%) region and the main (20% to 80%) region at 25-Hz flapping.

Wing	Mid-downstroke period		Mid-upstroke period	
	Torsion from 0% to 20% of wing length	Torsion from 20% to 80% of wing length	Torsion from 0% to 20% of wing length	Torsion from 20% to 80% of wing length
HBH	5.7° (100%)	20.9° (100%)	−2.7° (100%)	−26.8° (100%)
Non-torsion	4.0° (70%)	13.5° (65%)	−2.9° (107%)	−15.1° (56%)
Non-stretch	6.9° (121%)	17.2° (82%)	−4.0° (148%)	−18.2° (68%)
Hummingbird [15]	-	23.2° (111%)	-	−47.5° (177%)

period between the two wings (Table 5), which might be caused by the asymmetry of the wing structure.

It was found that the magnitude of the angle of attack at the end of each mid-stroke period was larger than that of the beginning of the period (t = 0.175T or 0.2T; t = 0.675T or 0.67T) (Fig. 8). It is assumed to be because the wing speed reaches its highest value at the near start of each mid-stroke period (t = 0.15T or 0.175T; t = 0.655T or 0.675T), followed by deceleration of wing velocity (Fig. 9). That is, the reduction in the wing speed led to a decrease in aerodynamic force, leading to less twist too. Therefore, controlling the angular velocity of the flapping machine to maintain the wing speed may keep the twist and generate more lift.

E. Comparison of deformation and angle of attack with hummingbird wing

Comparing the twist from the 20% to 80% positions of the wing length of the HBH wing and the actual hummingbird [15], the hummingbird showed 11% larger twist in the mid-downstroke period and 77% larger twist in the mid-upstroke period than the HBH wing (Table 5).

As for the average angle of attack, the value for the hummingbird was 5° larger than that of the HBH wing in the mid-downstroke period at all wing length positions (Table 7). On the other hand, the hummingbird had a larger twist in the Mid-upstroke period, and the angle of attack at 20% of the wing length was larger than that of the HBH wing but smaller at 80% of the wing length (Table 7). This suggests that the asymmetry between the mid-upstroke period and the mid-downstroke period was smaller for the artificial wing and that the wing was able to generate a more stable downwash with either stroke.

IV. Conclusion

In this study, a hybrid wing consisting of a hummingbird-inspired torsional arm and a bat-inspired stretchable membrane was fabricated by 3-D printing aiming to realize hummingbird-like wing twists during flapping. The wing was flapped using an electric flapping mechanism to evaluate the wing twist and lift generation performance in hummingbird-like hovering. The torsional arm promoted the wing twist, while the stretchable membrane further enhanced the twist effect of the torsional arm. The membrane also created positive camber during each stroke. As result, the wing improved the efficacy of lift generation defined as lift per input power by more than 8% at 25 Hz compared with the wings with non-torsional arm or non-stretchable membrane. On the other hand, the lift was moderate, which was 3% smaller than the other wings at most at 25 Hz. The present study demonstrated the effectiveness of the hybrid approach in the design of bioinspired wings.

Table 6 Average camber ratio at 80% wing length position.

Wing	Mid-downstroke period	Mid-upstroke period
HBH	13.9%	11.6%
Non-torsion	12.2%	12.7%
Non-stretch	9.0%	7.6%
Hummingbird [15]	5.4%	3.9%

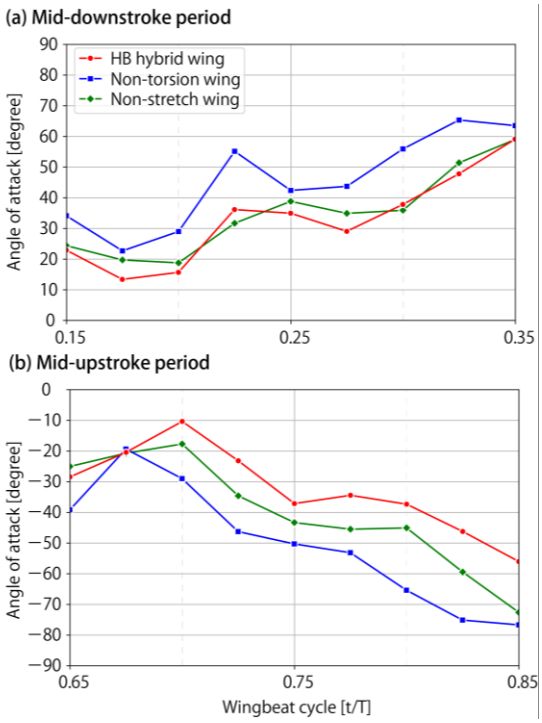

Figure 8 Time variation of angles of attack at 80% wing length position.

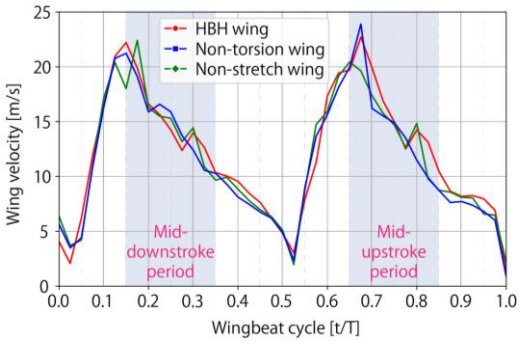

Figure 9 Wing velocity at wing length 80%.

Table 7 Average angle of attack at each wing length positions.

Wing	Mid-downstroke period			Mid-upstroke period		
	Wing length 20%	Wing length 50%	Wing length 80%	Wing length 20%	Wing length 50%	Wing length 80%
HBH	39.2°	31.8°	24.9°	−46.1°	−34.5°	−28.4°
Non-torsion	41.0°	35.5°	37.9°	−55.7°	−48.8°	−47.9°
Non-stretch	40.3°	33.6°	28.2°	−52.5°	−46.3°	−40.5°
Hummingbird* [15]	46.3°	45.6° / 39.4°	30.2°	−58.6°	−38.1° / −30.0°	−18.2°

* Because there is no data for the 50% position of the wing length, the data for 40% and 60% are listed from left to right.

REFERENCES

[1] Y. Nan, M. Karásek, M. E. Lalami, and A. Preumont, "Experimental optimization of wing shape for a hummingbird-like flapping wing Micro Air Vehicle," *Bioinspiration & Biomimetics*, vol. 12, no. 2, 026010, 2017.

[2] M. Keennon, K. Klingebiel, and H. Won, "Development of the nano hummingbird: A tailless flapping wing Micro Air Vehicle," *50th AIAA Aerospace Sciences Meeting including the New Horizons Forum and Aerospace Exposition*, 2012.

[3] D. Coleman, M. Benedict, V. Hirishikeshaven, and I. Chopra, "Development of a robotic hummingbird capable of controlled hover," *Journal of the American Helicopter Society*, vol. 62, no. 3, pp. 1–9, 2017.

[4] T. Nakata, H. Liu, Y. Tanaka, N. Nishihashi, X. Wang, and A. Sato, "Aerodynamics of a bio-inspired flexible flapping-wing Micro Air Vehicle," *Bioinspiration & Biomimetics*, vol. 6, no. 4, 045002, 2011.

[5] H. V. Phan, S. Aurecianus, T. K. Au, T. Kang, and H. C. Park, "Towards the long-endurance flight of an insect-inspired, tailless, two-winged, flapping-wing flying robot," *IEEE Robotics and Automation Letters*, vol. 5, no. 4, pp. 5059–5066, 2020.

[6] K. Y. Ma, P. Chirarattananon, S. B. Fuller, and R. J. Wood, "Controlled flight of a biologically inspired, insect-scale robot," *Science*, vol. 340, no. 6132, pp. 603–607, 2013.

[7] H. V. Phan, Q. V. Nguyen, Q. T. Truong, T. V. Truong, H. C. Park, N. S. Goo, D. Byun, and M. J. Kim, "Stable vertical takeoff of an insect-mimicking flapping-wing system without guide implementing inherent pitching stability," *Journal of Bionic Engineering*, vol. 9, no. 4, pp. 391–401, 2012.

[8] G. C. de Croon, M. A. Groen, C. De Wagter, B. Remes, R. Ruijsink, and B. W. van Oudheusden, "Design, aerodynamics and autonomy of the DelFly," *Bioinspiration & Biomimetics*, vol. 7, no. 2, 025003, 2012.

[9] K. Y. Ma, P. Chirarattananon, S. B. Fuller, and R. J. Wood, "Controlled flight of a biologically inspired, insect-scale robot," *Science*, vol. 340, no. 6132, pp. 603–607, 2013.

[10] A. Ramezani, S.-J. Chung, and S. Hutchinson, "A biomimetic robotic platform to study flight specializations of bats," *Science Robotics*, vol. 2, no. 3, eaal2505, 2017.

[11] K. Peterson, P. Birkmeyer, R. Dudley, and R. S. Fearing, "A wing-assisted running robot and implications for avian flight evolution," *Bioinspiration & Biomimetics*, vol. 6, no. 4, 046008, 2011.

[12] T. Nakata, R. Noda, and H. Liu, "Effect of twist, camber and spanwise bending on the aerodynamic performance of flapping wings," *Journal of Biomechanical Science and Engineering*, vol. 13, no. 2, 17-00618, 2018.

[13] A. Hedenström and L. C. Johansson, "Bat flight: Aerodynamics, kinematics and flight morphology," *Journal of Experimental Biology*, vol. 218, no. 5, pp. 653–663, 2015.

[14] D. R. Warrick, B. W. Tobalske, and D. R. Powers, "Aerodynamics of the hovering hummingbird," *Nature*, vol. 435, no. 7045, pp. 1094–1097, 2005.

[15] M. Maeda, T. Nakata, I. Kitamura, H. Tanaka, and H. Liu, "Quantifying the dynamic wing morphing of hovering hummingbird," *Royal Society Open Science*, vol. 4, no. 9, 170307, 2017.

[16] T. L. Hedrick, B. W. Tobalske, I. G. Ros, D. R. Warrick, and A. A. Biewener, "Morphological and kinematic basis of The hummingbird flight stroke: Scaling of flight muscle transmission ratio," *Proceedings of the Royal Society B: Biological Sciences*, vol. 279, no. 1735, pp. 1986–1992, 2011.

[17] J. A. Cheney, J. C. Rehm, S. M. Swartz, and K. S. Breuer, "Bats actively modulate membrane compliance to control camber and reduce drag," *Journal of Experimental Biology*, vol. 225, no. 14, jeb243974, 2022.

[18] H. Tanaka, T. Nakata, and T. Yamasaki, "Biomimetic Soft Wings For Soft Robot Science," *Journal of Robotics and Mechatronics*, vol. 34, no. 2, pp. 223–226, 2022.

[19] A. Kawahara, M. Aizawa, T. Yamasaki, and H. Tanaka, "Fabrication of a Hummingbird-mimetic Flexible Flapping Wings," *in 30th 2019 International Symposium on Micro-NanoMechatronics and Human Science*, pp. 138–140, 2019.

[20] A. P. Boresi, K. P. Chong, and J. D. Lee, Elasticity in engineering mechanics. Hoboken, N.J: Wiley, 1987, pp. 570–574.

[21] M. H. Sadd, Elasticity: Theory, applications, and numerics. Erscheinungsort nicht ermittelplate: Academic Press Inc, 2009, pp. 233–235.

[22] Y. Nan, M. Karásek, M. E. Lalami, and A. Preumont, "Experimental optimization of wing shape for a hummingbird-like flapping wing Micro Air Vehicle," *Bioinspiration & Biomimetics*, vol. 12, no. 2, 026010, 2017.

[23] H. Tanaka, H. Suzuki, I. Kitamura, M. Maeda, and Hao Liu, "Lift generation of hummingbird wing models with flexible loosened membranes," *2013 IEEE/RSJ International Conference on Intelligent Robots and Systems*, pp. 3777–3783, 2013.